Electron-impact excitation of low-lying preionization-edge electronic and Rydberg transitions of fluoroform and chloroform: Bethe surfaces and absolute generalized oscillator strengths

J. F. Ying* and K. T. Leung†
Department of Physics and Department of Chemistry, The University of Waterloo, Waterloo, Ontario, Canada N2L 3G1
(Received 25 July 1995)

Absolute generalized oscillator strengths (GOSs) of valence-shell electronic transitions of CHF_3 and $CHCl_3$ as functions of energy loss (0–150 eV) and momentum transfer (i.e., the Bethe surfaces) have been determined using angle-resolved electron energy-loss spectroscopy at an impact energy of 2.5 keV. The assignments for the prominent low-lying preionization-edge energy-loss features of CHF_3 and $CHCl_3$ were inferred from the term values reported previously and from their characteristic experimental GOS profiles. In particular, the GOS profiles of the low-lying Rydberg transitions (which originated from the nonbonding highest occupied molecular orbitals) below the ionization edge at 11.1, 11.9, 12.7, and 13.7 eV in CHF_3 and at 8.5, 9.6, and 10.6 eV in $CHCl_3$ were determined. These GOS profiles were found to be dominated by a strong maximum at zero-momentum transfer, which is characteristic of dipole interaction. Weak secondary maxima (and minima) were also observed and could be interpreted qualitatively in terms of the spatial overlaps between the initial-state and final-state orbital wave functions. In addition, the low-lying feature at 7.2 eV in $CHCl_3$ could be attributed predominantly to electronic excitations from the Cl $3p$ nonbonding (n) orbitals ($2a_2$, $9e$, $9a_1$, and $8e$) to a C-Cl σ^* antibonding orbital ($10a_1$), according to a single-excitation configuration-interaction (CI) excited-state calculation. The experimental GOS profile of this low-lying feature was found to have a shape that is characteristic of a mixture of dipole-allowed and nondipole interactions, with maxima at momentum transfers of 0 and ~0.9 a.u., respectively. Furthermore, the CI calculation indicated that some of these $n(\text{Cl } 3p)\rightarrow\sigma^*(\text{C-Cl})$ excitations in $CHCl_3$, like other Cl-containing freons [CF_nCl_{4-n} ($n=0$–3) and CHF_mCl_{3-m} ($m=1,2$)], could also lead to dissociation of the C-Cl bond.

PACS number(s): 34.80.Gs

I. INTRODUCTION

The large-scale consumption of chlorofluorocarbons (CFCs) or freons (as refrigerants, aerosol propellants, and semiconductor etchants, etc.) in many industrial applications [1,2] is of particular environmental concern because of their destructive effect on ozone in the stratosphere. Many of the popular CFCs, such as CF_nCl_{4-n} ($n=0$–4), are being replaced with ''temporary'' substitutes, which usually contain a hydrogen replacement of a chlorine atom, i.e., chlorofluorohydrocarbons (CFHCs) such as CHF_mCl_{3-m} ($m=0$–3) and their derivatives. Unlike CF_nCl_{4-n} ($n=0$–4) [3,4], however, the electronic structure and photochemistry of CHF_mCl_{3-m} ($m=0$–3) are less well understood. For instance, there is no information on the important excitation cross sections [or generalized oscillator strengths (GOSs)] of low-lying or any other electronic transitions, which may play a key role in the relevant atmospheric and industrial processes. It was only recently that we reported a GOS study of low-lying preionization-edge electronic transitions of CF_4 and CCl_4 [5], and of CF_3Cl, CF_2Cl_2, and $CFCl_3$ [6] by using angle-resolved electron energy-loss spectroscopy (EELS). In particular, absolute GOS measurements of low-lying electronic transitions from the Cl $3p$ nonbonding orbitals [n(Cl $3p$)] to a σ^*(C-Cl) antibonding orbital in CF_nCl_{4-n} ($n=0$–3) [5–7] (and in CHF_2Cl [8]) showed that these $n(\text{Cl } 3p)\rightarrow\sigma^*(\text{C-Cl})$ transitions are predominantly due to a quadrupole interaction that resembles that of an atomic $p\rightarrow p$ transition in a Cl atom, and that some of these transitions may subsequently lead to dissociation of the C-Cl bond. A few of these $n\rightarrow\sigma^*$ transitions in the 6–9-eV region for some of the more common CFC and CFHC molecules have also been reported as ''weak'' features in the early vacuum ultraviolet (VUV) photoabsorption [9] and small-angle high-resolution EELS studies [10]. We now present GOS data on similar low-lying preionization-edge features for the monohydrogen derivatives of CF_4 and CCl_4, i.e., fluoroform (CHF_3) and chloroform ($CHCl_3$), in an attempt to gain further insights into their electronic excitation structures. This type of comparative study is of particular interest to elucidating the effects of halogen content and symmetry change from T_d (as in CF_4 and CCl_4) to C_{3v} (as in CHF_3 and $CHCl_3$) on the GOS profiles and the nature of this type of $n\rightarrow\sigma^*$ and other electronic excitations.

Absolute GOS measurement by using angle-resolved EELS provides quantitative information on both dipole-allowed and nondipole transitions and gives insights into the nature of the underlying interactions. In particular, nondipole transitions that are not easily accessible to optical techniques have been discovered using angle-resolved EELS in the valence-shell regions of N_2 [11], O_2, CO, NO, CO_2, N_2O [12], C_2H_2 [13], benzene [14], and p-difluorobenzene [15], as well as more recently in the inner-shell regions of N_2, NO, N_2O [16], CO_2 [17], and SF_6 [18]. The GOS is defined as [19]:

*Present address: Department of Chemistry, University of British Columbia, Vancouver, British Columbia, Canada V6T 1Z1.
†Author to whom correspondence should be addressed. Electronic address: Tong@UWaterloo.ca

$$f(K,E)=\frac{E}{K^2}\left|\langle\Psi_n|\sum_{j=1}^{N}\exp(i\mathbf{K}\cdot\mathbf{r}_j)|\Psi_0\rangle\right|^2, \qquad (1)$$

where Ψ_0 and Ψ_n are the (N-electron) electronic wave functions of the initial (ground) and final states, respectively, and $\mathbf{r}_j$ is the position of the jth electron with respect to the center of mass of the target. The GOS profile (over an extended range of momentum transfer K) of an individual transition is directly related to the initial-state and excited-state wave functions and hence the nature of the underlying interaction. For instance, it is possible to infer the qualitative nature of the transition of interest and to facilitate its spectral assignment by examining the GOS profile. In favorable cases where *ab initio* GOS calculations are available, more rigorous verification of the assignment can be achieved by comparing both the shape and absolute magnitude of the GOS profile between experiment and theory. The usefulness of the GOS technique has been clearly demonstrated in the studies of the Lyman-Birge-Hopfield band in N_2 [11] and, more recently, of the $n\rightarrow\sigma^*$ transitions in CFCs and CFHCs, including the $7e\rightarrow 11a_1$ transition at 7.7 eV in CF_3Cl [7], the $(7a'',14a')\rightarrow 15a'$ transitions at 8.0 eV in CHF_2Cl [8], the $(8b_2,3a_2)\rightarrow 13a_1$ transitions at 6.9 eV and $(6b_1,12a_1)\rightarrow 13a_1$ transitions at 8.1 eV in CF_2Cl_2, as well as the $(2a_2,10e)\rightarrow 12a_1$ transitions at 6.8 eV and $(9e,11a_1)\rightarrow 12a_1$ transitions at 7.7 eV in $CFCl_3$ [6]. Furthermore, absolute measurement of the GOS profile of a particular transition can also be used for modeling the wave function, particularly that of the excited state if the ground-state wave function is known.

In addition to the study of nondipole phenomena, the GOS profiles of discrete electronic excitations, particularly Rydberg transitions, exhibit interesting secondary extrema (minima and maxima). Possible spectroscopic applications of the trends in the K positions of the minima have been suggested by Miller [20] in a systematic survey of the extrema in the GOS profiles of atomic transitions [21]. Minima in the GOS profiles of low-lying discrete molecular transitions with Rydberg character have been reported in H_2O [22,23], C_2H_4 [24], and NH_3 [25]. Only a very limited number of theoretical studies on the GOS minima of molecular transitions are available [22,26]. The origin of the extrema in the GOS profiles of molecular transitions is clearly more complicated, because the minima (and maxima) could come from not only the nodal structures of the initial-state and final-state wave functions (as in the case of atoms [27,28]) but also diffraction effects [29]. Systematic experimental and theoretical GOS studies of both valence and Rydberg transitions are obviously needed in order to further understand the significance of these GOS extrema and to explore their possible spectroscopic applications for specific types of transitions. Although various semiempirical trends involving the extrema may exist for a related set of molecular transitions, the assignment of a particular transition can be more reliably made by using GOS calculations with accurate wave functions. In the present work, we compare the secondary extrema in the GOS profiles of low-lying preionization-edge Rydberg transitions in CHF_3 and $CHCl_3$ with those of the corresponding transitions in CF_4 and CCl_4 [5].

II. EXPERIMENTAL DETAILS

The angle-resolved electron energy-loss spectrometer and experimental procedure used in the present work have been given in detail elsewhere [30]. Briefly, a collimated electron beam was accelerated to an impact energy of 2.5 keV and crossed with a gas jet expanded from a nozzle (0.5 mm diameter) positioned 1 cm above the collision center. Electrons scattered with an energy loss E at a scattering angle θ (from the forward direction) were energy analyzed using a hemispherical energy analyzer equipped with a seven-element input lens. Our spectrometer was capable of an overall energy resolution of 0.8 eV full width at half maximum (FWHM) and an angular resolution of 0.5° half angle. Valence-shell EELS spectra were collected at a series of θ angles from 1° to 10° in steps of 0.5° (corresponding to different K values) sequentially in repetitive scans. EELS spectra of the background gas (i.e., without the sample) were also recorded in the same energy loss and angular ranges after each measurement of the sample. These ''background'' spectra corresponding to the residual ambient gas were then removed from the corresponding sample spectra. The experimental relative cross section in the background-subtracted EELS spectra was converted to relative GOS using the Bethe-Born formula, which in Rydberg atomic units can be written as [19]

$$\frac{d^2\sigma}{d\Omega\,dE}=\frac{k}{k_0K^2}\frac{4}{E}\frac{df(K,E)}{dE}, \qquad (2)$$

where $d\Omega$ is the detection solid angle, E is the energy loss; $\mathbf{k}_0$ and $\mathbf{k}$ are the momenta of the incident and scattered electrons, respectively, and $\mathbf{K}$ ($=\mathbf{k}_0-\mathbf{k}$) is the momentum transfer. Because the EELS spectra were collected in a relatively normalized fashion, the entire relative GOS data could be put on an absolute scale by applying the Bethe-sum-rule normalization to a Bethe-Born-corrected EELS spectrum collected at a single K value [31]:

$$\int\frac{df(K,E)}{dE}\,dE=N, \qquad (3)$$

where N is the total number of electrons in the target. In the Bethe-sum-rule normalization procedure, the intensity of the relative GOS obtained at the lowest K value for the valence shell was numerically integrated over the sampling range of energy loss, i.e., up to $E=150$ eV for both CHF_3 and $CHCl_3$. The remaining intensity for the valence shell above 150 eV was estimated by integrating a fitted function $B(E)$ ($=A/E^{\nu}$) from 150 eV to ''infinity'', with the empirical constants A and ν obtained by fitting $B(E)$ to the experimental GOS in the range 80–150 eV [32,33]. The sum of these two integrated intensities was then normalized to a total oscillator strength of 26.9, which corresponds to 26 valence-shell electrons plus a correction of 0.9 to account for the contribution due to Pauli-excluded transitions from the inner shells [34], for CHF_3 and $CHCl_3$.

Fluoroform (98% minimum purity) and chloroform (99.9% minimum purity) were purchased from Aldrich Chemical and Fisher Chemical, respectively, and were used without further purification. In the case of $CHCl_3$, the liquid sample was degassed before use by repeated freeze-pump-

thaw cycles. The ambient pressure of the chamber was maintained at $(1–2)\times10^{-5}$ Torr during the experiment, and the pressure at the collision region was estimated to be at least an order of magnitude higher. EELS spectra were also collected at different pressures to assure that multiple scattering effects were unimportant. Energy calibration was obtained by comparing the energy positions of the dominant dipole features in our near-zero-angle EELS spectra with, wherever available, literature optical data (see below).

III. RESULTS AND DISCUSSION

A. Ground-state electronic configurations and Bethe surfaces of CHF_3 and $CHCl_3$

The ground-state electronic configurations for the valence shells of CHF_3 and $CHCl_3$, obtained with a 6-31G basis set and internally optimized geometries by self-consistent-field (SCF) calculations using a commercial program GAUSSIAN 90 [35], are

$$CHF_3: \quad X\,^1A_1-(3a_1)^2(2e)^4(4a_1)^2(5a_1)^2(3e)^4[(4e)^4(5e)^4(1a_2)^2(6a_1)^2]_{n(\mathrm{F}\ 2p)}[(7a_1)^0]_{\sigma^*(\mathrm{C\text{-}F})}[(6e)^0]_{\pi^*(\mathrm{C\text{-}F})}\cdots,$$

$$CHCl_3: \quad X\,^1A_1-(6a_1)^2(6e)^4(7a_1)^2(8a_1)^2(7e)^4[(8e)^4(9a_1)^2(9e)^4(2a_2)^2]_{n(\mathrm{Cl}\ 3p)}[(10a_1)^0]_{\sigma^*(\mathrm{C\text{-}Cl})}[(10e)^0]_{\pi^*(\mathrm{C\text{-}Cl})}\cdots .$$

The configurations are consistent with the corresponding photoelectron results for CHF_3 [36] and $CHCl_3$ [37]. It should be noted that although the four highest occupied molecular orbitals (HOMOs) are predominated by nonbonding p orbitals from the halogen atoms, there are minor contributions from, e.g., σ bonding between C and H in the $6a_1$ orbital of CHF_3 and in the $9a_1$ orbital of $CHCl_3$. Furthermore, the lowest unoccupied molecular orbitals (LUMOs) of CHF_3 and $CHCl_3$ are both of a_1 symmetry and mainly composed of σ^* antibonding between C and the halogen.

The dependence of the absolute GOSs of individual electronic transitions on the energy loss and momentum transfer can be best summarized in a Bethe surface plot. The Bethe surface contains important information about the inelastic electron scattering process within the first Born approximation, and is particularly useful for analyzing such quantities as stopping power, total inelastic scattering cross section, and polarizability [19]. Figure 1 shows the Bethe surfaces of CHF_3 and $CHCl_3$ in two different perspectives of the electron-molecule scattering process. In particular, Fig. 1(a) [1(c)] focuses on ''close'' collisions, which correspond to the impact-scattering region of large momentum transfer (and energy loss) [19]. In this region, a broad ridge (corresponding to the Bethe ridge under the conditions of the Born approximation) arises as a result of momentum conservation in the inelastic electron-molecule scattering process, and is found to disperse to a higher energy loss with increasing momentum transfer. On the other hand, Fig. 1(b) [1(d)] emphasizes ''distant'' collisions, which correspond to the dipole-scattering (''pseudo-optical'') region of small momentum transfer (and energy loss) [19]. The Bethe surface of $CHCl_3$ [Fig. 1(d)] is evidently more concentrated in the dipole-scattering region than that of CHF_3 [Fig. 1(b)], giving rise to a more rapid dropoff in the K direction of the Bethe surface. A similar trend in the Bethe surfaces of CF_nCl_{4-n} ($n=0–4$) has been observed in our previous studies [5,6]. The higher GOS concentration at the lower energy loss and lower momentum transfer region (as in $CHCl_3$ relative to that of CHF_3) can be qualitatively correlated with, respectively, the increasingly lower ionization potentials and more diffuse orbitals due to increased chlorination. The rapid dropoff in the oscillator strength with energy from F to Cl has also been illustrated by Manson *et al.* in their theoretical study of the photoionization cross sections of halogen atoms [38].

B. Angle-resolved EELS spectra of CHF_3 and $CHCl_3$

Figures 2 and 3 show a selected set of EELS spectra measured at 1°, 3°, 5°, 7°, and 9° for CHF_3 and $CHCl_3$, respectively. The vertical ionization potentials (IPs) obtained by photoelectron spectroscopy [36,37] for the valence-shell $(X,A-H)$ ionic states, along with the term values for the

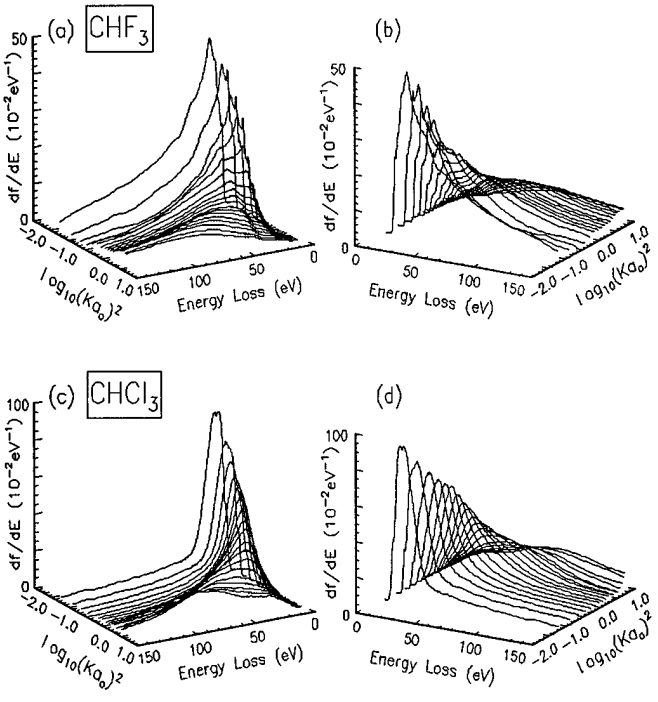

FIG. 1. Bethe surfaces of the valence shells of CHF_3 [(a) and (b)] and $CHCl_3$ [(c) and (d)] determined at 2.5-keV impact energy. EELS spectra are collected in steps of 0.5° from 1.0° to 9.5° for both CHF_3 and $CHCl_3$. The spectra have been smoothed for clarity. The impact-scattering (large momentum transfer) region is emphasized in (a) and (c) while the dipole-scattering (small momentum transfer) region is emphasized in (b) and (d).

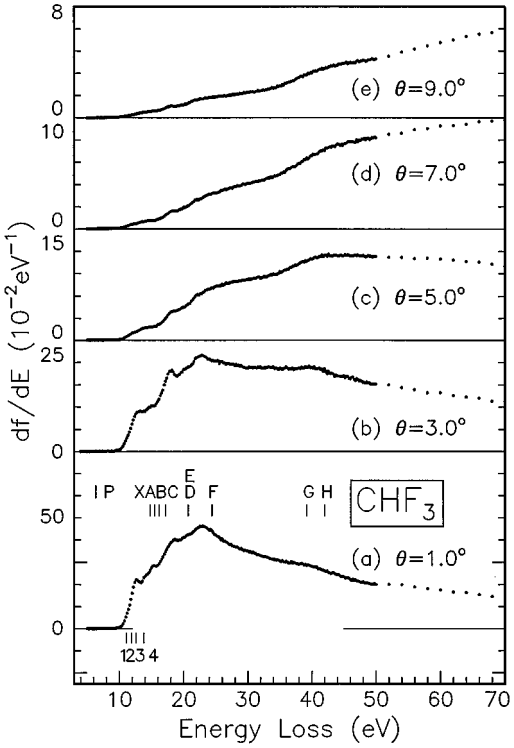

FIG. 2. Valence-shell absolute angle-resolved electron energy-loss spectra of CHF_3 measured at (a) 1.0°, (b) 3.0°, (c) 5.0°, (d) 7.0°, and (e) 9.0°. The vertical ionization potentials (IPs) corresponding to the ionic states X: $(6a_1)^{-1}$, A: $(1a_2)^{-1}$, B: $(5e)^{-1}$, C: $(4e)^{-1}$, D: $(3e)^{-1}$, E: $(5a_1)^{-1}$, F: $(4a_1)^{-1}$, G: $(2e)^{-1}$, and H: $(3a_1)^{-1}$ are taken from Ref. [36]. Plausible assignments for the numbered features are given in Table III.

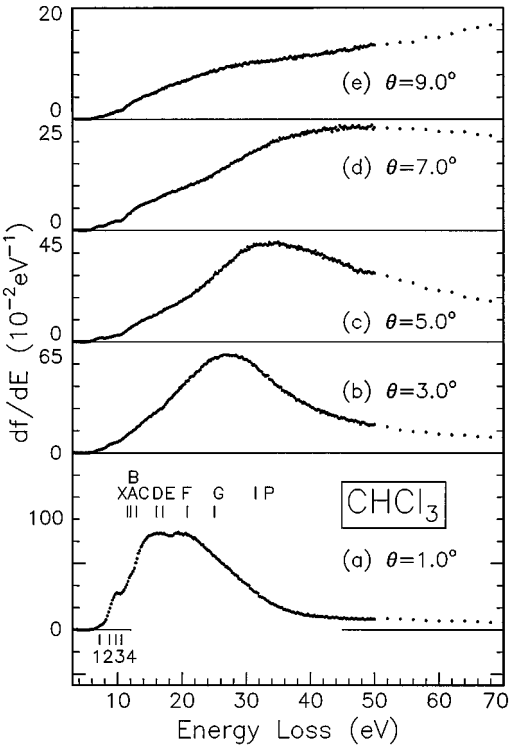

FIG. 3. Valence-shell absolute angle-resolved electron energy-loss spectra of $CHCl_3$ measured at (a) 1.0°, (b) 3.0°, (c) 5.0°, (d) 7.0°, and (e) 9.0°. The vertical ionization potentials (IPs) corresponding to the ionic states X: $(2a_2)^{-1}$, A: $(9e)^{-1}$, B: $(9a_1)^{-1}$, C: $(8e)^{-1}$, D: $(7e)^{-1}$, E: $(8a_1)^{-1}$, F: $(7a_1)^{-1}$, and G: $(6e)^{-1}$ are taken from Ref. [37]. Plausible assignments for the numbered features are given in Table IV.

unoccupied orbitals obtained from valence-shell EELS [39] and C K-shell photoabsorption measurements for CHF_3 [40] and from C $1s$ and Cl $2p$ EELS study [41] for $CHCl_3$, are also given in Tables I and II, respectively. It is well known that under the conditions of vanishingly small scattering angle and high impact energy (i.e., the dipole-scattering condition), the GOS converges to the dipole oscillator strength (DOS) [19], which has been traditionally obtained by photoabsorption spectroscopy. Unlike CF_4 and CCl_4, for which a considerable amount of photoabsorption and EELS data are available (see, e.g., Ref. [5]), only limited information on CHF_3 and $CHCl_3$ can be found in the literature. In the case of CHF_3, Stokes and Duncan [42] and Sauvageau *et al.* [43] reported VUV photoabsorption spectra from 10 to 18 eV, while Harshbarger, Robin, and Lassettre gave a corresponding EELS spectrum (8–22 eV) obtained at 400-eV impact energy and 0° scattering angle [39]. Although none of these higher-resolution spectra provides absolute oscillator strengths, these spectra give useful information on the energy positions of the observed lines, which are found to be in good accord with our "absolute" EELS spectrum measured at 1° [Fig. 2(a)]. Furthermore, the absolute photoabsorption cross section of CHF_3 from 10.5 to 25 eV obtained by Lee *et al.* using synchrotron radiation [44] is also found to be in excellent agreement with our 1° spectrum, after differences in the energy resolutions and small variations in the absolute intensity due to the small scattering angle are taken into account. To the best of our knowledge, even less information on the electronic excitation of $CHCl_3$ is available in the literature. In particular, only the line positions for the VUV photoabsorption features in the 7–11-eV region were reported by Zobel and Duncan [45]. Figure 3(a) therefore represents, to our knowledge, the first detailed (absolute) "photoabsorption" spectrum reported to date.

Some of the more prominent preionization-edge features have been identified based on the previous VUV photoab-

TABLE I. Experimental vertical ionization potentials (IPs) of the occupied valence orbitals and term values of the unoccupied virtual orbitals of CHF_3.

Occupied orbital	IP (eV) Ref. [36]	Virtual orbital	Term value (eV) Ref. [39]	Ref. [40][a]
$6a_1$ (HOMO)	14.8	$4s$	1.48–1.70	1.9
$1a_2$	15.5	$3p$	2.55–3.44	3.8
$5e$	16.2	$3s$	3.59–4.42	4.3
$4e$	17.2	$6e$		
$3e$	20.7	$7a_1$ (LUMO)		
$5a_1$	20.7			
$4a_1$	24.4			
$2e$	39.2			
$3a_1$	42.0			

[a]The C K-shell photoabsorption data given by Brown *et al.* [40] have been reinterpreted.

TABLE II. Experimental vertical ionization potentials (IPs) of the occupied valence orbitals and term values of the unoccupied virtual orbitals of $CHCl_3$.

Occupied orbital	IP (eV) Ref. [37]	Virtual orbital	Term value (eV) Ref. [41][a]
$2a_2$ (HOMO)	11.5	$5s$	1.8
$9e$	12.0	$4p$	2.4 (3.5, 3.1)
$9a_1$	12.0	$4s$	(4.4, 5.1)
$8e$	12.9	$10e$	5.0
$7e$	16.0	$10a_1$ (LUMO)	3.9, 5.8 (6.2)
$8a_1$	17.0		
$7a_1$	20.8		
$6e$	25		
$6a_1$			

[a]The term values are derived from the excitation features in the C $1s$ and Cl $2p$ shells (in parentheses) obtained by small-angle EELS.

sorption [42,45] and EELS [39] studies and are labeled as Features 1–4 in Figs. 2 and 3. The transition energies and assignments of the preionization-edge features for CHF_3 and $CHCl_3$ are given in Tables III and IV, respectively. In particular, both Stokes and Duncan [42] and Harshbarger, Robin, and Lassettre [39] assigned all of the observed features in CHF_3 entirely to Rydberg transitions. However, since, as noted by Sauvageau *et al.* [43], the assignments by Stokes and Duncan were made at the time when the IPs were not known precisely, we therefore favor the assignments made by Harshbarger, Robin, and Lassettre (Table III). Given the lack of any notable angular variations that are characteristic of nondipole behavior in the observed features in our angle-resolved EELS spectra of CHF_3 (Fig. 2), it is difficult to infer additional assignments. The prominent features observed above the ionization limit are consistent with the expected Rydberg transitions converging to the reported ionization edges of the ionic states. In the case of $CHCl_3$, we are able to supplement the qualitative assignment made by Zobel and Duncan [45] with the tentative assignments shown in Table IV, by using the IPs and term values given in Table II. Because there is no notable nondipole behavior except for feature 1 (see below), we favor assignments that involve dipole transitions, although nondipole transitions cannot be ruled out. The corresponding term values derived from the proposed assignments are found to be in good accord with those obtained from an earlier inner-shell EELS study [41]. It should be noted that the term values of the Rydberg orbitals are transferable from the inner-shell transitions to the valence-shell transitions, while the term values of the virtual orbitals derived from the inner-shell transitions are always larger than those obtained from the valence-shell transitions due to a bigger relaxation effect in the inner shells [46].

The nature of the transitions associated with the low-lying preionization-edge features in Figs. 2 and 3 can be inferred by examining their GOS profiles. In particular, four Gaussian peaks were used to deconvolute the intensities of features 1–4 at the energy positions determined previously from high-resolution VUV photoabsorption studies (Tables III and IV), with the fifth Gaussian line shape used to simulate the onset of the first ionization edge (the X ionic state) and its nearby structure. The widths of the Gaussian peaks were obtained from the linewidths in the photoabsorption spectra, after taking the instrumental energy resolution into account. Typical Gaussian fits to the EELS spectra obtained at 5° for the preionization-edge features of CHF_3 and $CHCl_3$ are shown in Fig. 4. The GOSs of these preionization-edge features at a particular K value could be obtained by computing the areas under the corresponding Gaussian peaks. The resulting experimental GOS profiles have been fitted semiempirically using the Lassettre series [14,15,47]:

$$f(K,E)=\frac{1}{(1+x)^6}\sum_{n=0}^{5} f_n\left(\frac{x}{1+x}\right)^n, \tag{4}$$

where $x=K^2/[(2I)^{1/2}+(2|I-W|)^{1/2}]^2$, and W and I are the excitation energy of the discrete transition and the IP of the nearest ionic state, respectively. The parameters f_n in the Lassettre series are related to linear combinations of the respective multipole matrix elements, with f_0 corresponding to the DOS [47]. Since the general angular variations of the EELS spectra of CHF_3 (Fig. 2) and $CHCl_3$ (Fig. 3) are found to be notably similar to those of CF_4 and CCl_4, respectively (Figs. 4 and 5 in Ref. [5]), we expect similar behavior in the GOS profiles for the corresponding transitions. We shall first discuss the similarities in the GOS profiles of the low-lying Rydberg features between CHX_3 and CX_4 (X=F and Cl), and

TABLE III. Plausible assignments of the observed features in the angle-resolved EELS spectra of CHF_3.

	Energy loss (eV)			Assignment	
Feature	Ref. [42]	Ref. [39]	This work	Ref. [42][a]	Ref. [39][a]
1	11.04	10.92	11.1	$6a_1\rightarrow 3s$ [2.80]	$6a_1\rightarrow 3s$ [3.88]
2	11.84	11.95	11.9	$5e\rightarrow 3s$ [1.22]	$6a_1\rightarrow 3p$ [2.85]
3	12.63	12.58	12.7	$6a_1\rightarrow 4s$ [4.50]	$5e\rightarrow 3s$ [3.62]
4	13.79	13.65	13.7	$(6a_1)^{-1}$	$5e\rightarrow 3p$ [2.55]
					$4e\rightarrow 3s$ [3.59]
5	14.51	14.49		$5e\rightarrow 4s$ [1.83]	$4e\rightarrow 3p$ [2.75]
6		15.76			$4e\rightarrow 3d$ [1.48]
7		16.42			$(3e,5a_1)\rightarrow 3s$ [4.42]
8		17.40			$(3e,5a_1)\rightarrow 3p$ [3.44]
9		19.14			$(3e,5a_1)\rightarrow 3d$ [1.70]

[a]The term values (in units of eV) for the final-state orbitals are given in square brackets.

TABLE IV. Plausible assignments of the observed features in the angle-resolved EELS spectra of $CHCl_3$.

	Energy loss (eV)		Assignment	
Feature	Ref. [45]	This work	Ref. [45]	This work[a]
1	7.08	7.2	$n\rightarrow\sigma^*$(C—Cl)	$2a_2\rightarrow 10a_1$ [4.3]
				$(9a_1,9e)\rightarrow 10a_1$ [4.8]
				$8e\rightarrow 10a_1$ [5.7]
2	8.70	8.5	Rydberg	$8e\rightarrow 4s$ [4.4]
3	9.33		Rydberg (with possible	$(9a_1,9e)\rightarrow 4p$ [2.4]
	9.63	9.6	vibrational states)	$2a_2\rightarrow 5s$ [1.9]
	9.86			
4	10.62	10.6	Rydberg	$7e\rightarrow 4s$ [5.4]
				$8e\rightarrow 4p$ [2.3]

[a]Tentative assignments obtained from our angle-resolved energy-loss spectra are given here. The term values (in units of eV) for the final-state orbitals are given in square brackets.

then compare the GOS profiles of the low-lying n(Cl $3p$)$\rightarrow\sigma^*$(C-Cl) excitation features in $CHCl_3$ and CCl_4.

C. GOS profiles of preionization-edge Rydberg transitions in CHF_3 and $CHCl_3$

The GOS profiles of the low-lying preionization-edge features in CHF_3 at 11.1 (feature 1) and 11.9 eV (feature 2), and at 12.7 (feature 3) and 13.7 eV (feature 4) are shown in Figs. 5 and 6, respectively, and those of $CHCl_3$ at 8.5 (feature 2), 9.6 (feature 3), and 10.6 eV (feature 4) are shown in Fig. 7. Apparently, Rydberg transitions are believed to play a prominent role in the low-lying features below the first IPs in CHF_3 (Table III) and $CHCl_3$ (Table IV). In particular, the features at 11.1 (feature 1) and 11.9 eV (feature 2) in CHF_3 (Fig. 5) have been assigned to the $6a_1\rightarrow 3s$ and $6a_1\rightarrow 3p$ Rydberg transitions, respectively, by Harshbarger, Robin, and Lassettre [39]. The minor difference between the widths of these two features is likely caused by the different dipole components in the $6a_1$ orbital projected by the final-state orbitals. In addition, the more intense dipole peaks at 12.7 (feature 3) and 13.7 eV (feature 4) in CHF_3 have been assigned to $5e\rightarrow 3s$ and to $5e\rightarrow 3p$ and $4e\rightarrow 3s$ Rydberg transitions, respectively [39]. In the case of $CHCl_3$, the features at 8.5 (feature 2), 9.6 (feature 3), and 10.6 eV (feature 4) have all been designated as Rydberg transitions by Zobel and Duncan [45]. By considering the term values and the appro-

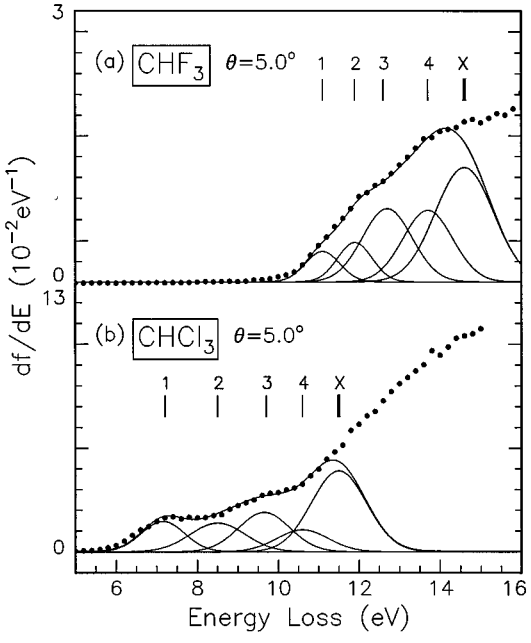

FIG. 4. Absolute angle-resolved electron energy-loss spectra illustrating the deconvolution procedure for determining the GOSs of (a) the preionization-edge features at 11.1 (feature 1), 11.9 (feature 2), 12.7 (feature 3), and 13.7 eV (feature 4) in CHF_3, and (b) those at 7.2 (feature 1), 8.5 (feature 2), 9.6 (feature 3), and 10.6 eV (feature 4) in $CHCl_3$.

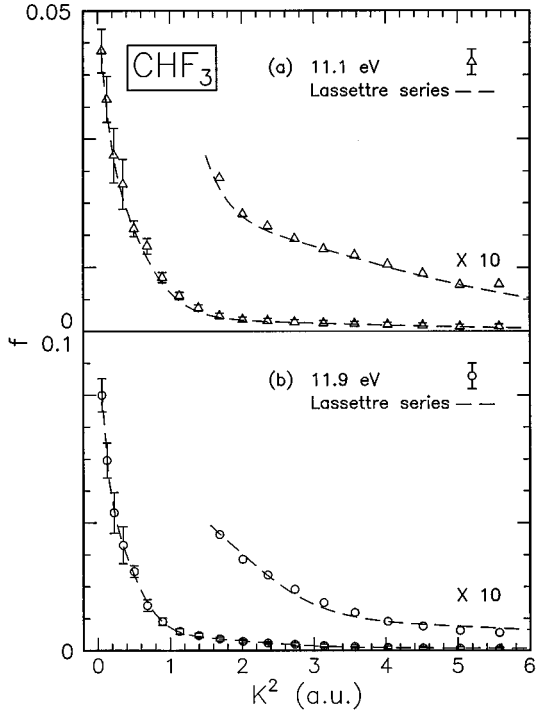

FIG. 5. Absolute generalized oscillator strength (f) as a function of momentum transfer (K) squared for the features at (a) 11.1 and (b) 11.9 eV in CHF_3. The dashed lines correspond to semiempirical fits using the Lassettre series.

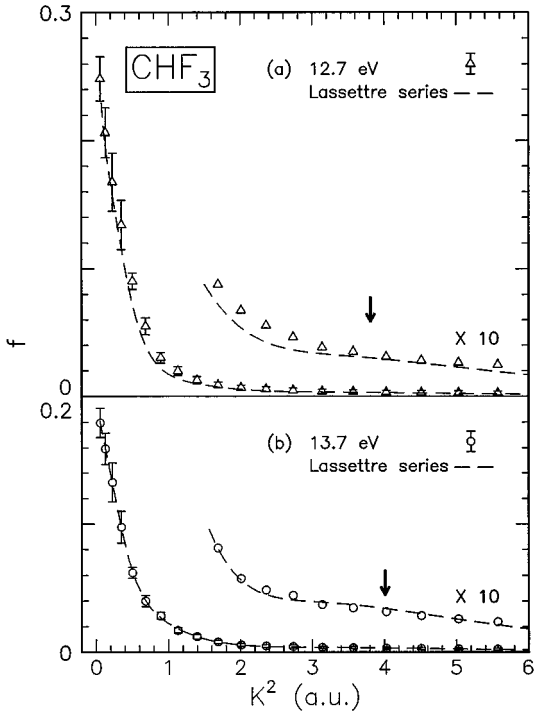

FIG. 6. Absolute generalized oscillator strength (f) as a function of momentum transfer (K) squared for the features at (a) 12.7 and (b) 13.7 eV in CHF_3. The dashed lines correspond to semiempirical fits using the Lassettre series.

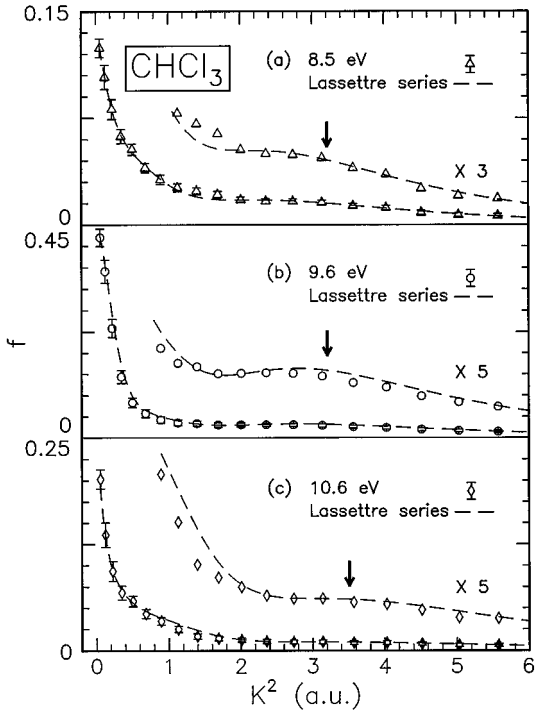

FIG. 7. Absolute generalized oscillator strength (f) as a function of momentum transfer (K) squared for the features at (a) 8.5, (b) 9.6, and (c) 10.6 eV in $CHCl_3$. The dashed lines correspond to semiempirical fits using the Lassettre series.

priate IPs, we may assign the features at 8.5 [Fig. 7(a)], 9.6 [Fig. 7(b)], and 10.6 eV [Fig. 7(c)] tentatively to the $8e\rightarrow 4s$, to $(9a_1,9e)\rightarrow 4p$ and $2a_2\rightarrow 5s$, and to $7e\rightarrow 4s$ and $8e\rightarrow 4p$ Rydberg transitions, respectively.

All of these profiles are dominated by a strong maximum at $K=0$, which is characteristic of the predominant dipole nature of the underlying transitions. Furthermore, weak secondary maxima at $K^2\sim 3.8$ and 4.0 a.u. and at $K^2\sim 3.2$, 3.2, and 3.5 a.u. are also evident in the GOS profiles of the CHF_3 features at 12.7 and 13.7 eV (Fig. 6) and in those of the $CHCl_3$ features at 8.5, 9.6, and 10.6 eV (Fig. 7), respectively. The secondary GOS maxima for the features at 12.7 and 13.7 eV in CHF_3 occur at essentially the same K position (given the large uncertainty in determining the maxima of these weak broad features). These secondary maxima are also found to be similar to those of the low-lying preionization-edge Rydberg features in CF_4 [5]. Similar observations can also be made for the secondary GOS maxima of the corresponding features in $CHCl_3$ and for their close resemblance to those in CCl_4 [5]. In the present work, care has been taken in performing the experiment at a sufficiently low ambient pressure to ensure that multiple scattering effects are unimportant in causing the observed secondary extrema. As in the case of CF_nCl_{4-n} ($n=0$–4) [5,6], the observed GOS secondary maxima (and minima) of the low-lying Rydberg features in CHF_3 and $CHCl_3$ may be qualitatively interpreted as manifestations of the spatial distributions (in Fourier space) of the overlap function between the relatively localized initial-state orbitals (corresponding usually to the nonbonding F $2p$ or Cl $3p$ orbitals) and the diffuse final-state Rydberg orbitals. Furthermore, the observed GOS secondary maxima for these low-lying Rydberg transitions in $CHCl_3$ (and in CF_3Cl, CF_2Cl_2, $CFCl_3$, and CCl_4) are found to be located at a lower K^2 value ($\sim$3.2–3.5 a.u.) than those of similar transitions in CHF_3 (and CF_4) (at $K^2\sim$3.8–4.0 a.u.), which may be attributed to the more diffuse nature of the nonbonding Cl $3p$ orbitals relative to F $2p$.

D. GOS profile of the low-lying $n\rightarrow\sigma^*$ feature at 7.2 eV in $CHCl_3$

Figure 8(a) shows the GOS profile of the preionization-edge excitation feature of $CHCl_3$ at 7.2 eV (feature 1 in Fig. 3). From a single-excitation CI excited-state calculation using a 6-31G basis set and an internally optimized geometry for $CHCl_3$ [35], we obtain the DOS values for transitions from the ground state ($^1A_1$) to the four lowest-lying excited states: $^1A_2$, ^1E, $^1A_1$, and ^1E, all with transition energies well within the experimental energy resolution of the observed peak maximum at 7.2 eV (Table V). It should be noted that only singlet-to-singlet electronic transitions are considered because the contributions from the spin-forbidden singlet-to-triplet transitions are expected to be small due to the high impact energy (2.5 keV) employed in the present experiment [48]. The major one-electron transitions for the $^1A_2$, ^1E, $^1A_1$, and ^1E excited states are, respectively, $2a_2\rightarrow 10a_1$, $9e\rightarrow 10a_1$, $9a_1\rightarrow 10a_1$, and $8e\rightarrow 10a_1$, all of which correspond to electronic transitions from the predominantly Cl $3p$ nonbonding orbitals to the C-Cl σ^* antibonding orbital (LUMO). Such a type of $n\rightarrow\sigma^*$ assignment is consistent with the assignment suggested by Zobel and Duncan [45] (Table IV) and with the previous assignments for the low-lying preionization-edge electronic excitation transitions in

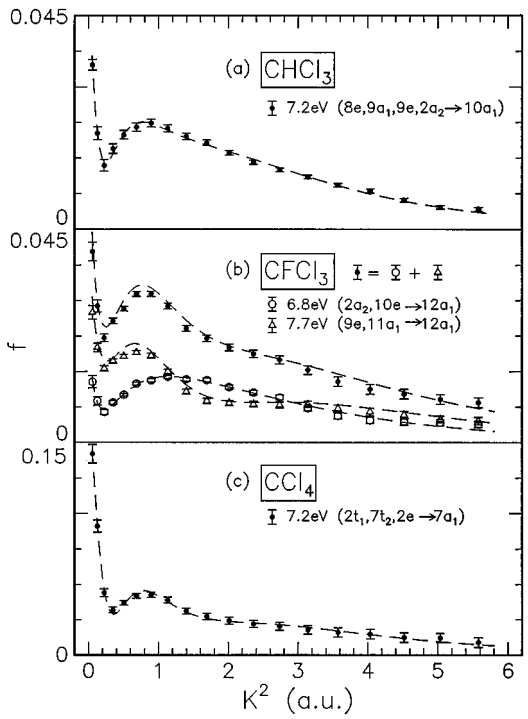

FIG. 8. Absolute generalized oscillator strength (f) as a function of momentum transfer (K) squared for the features at (a) 7.2 eV in $CHCl_3$, (b) 6.8 and 7.7 eV in $CFCl_3$ [6], and (c) 7.2 eV in CCl_4 [5]. The dashed lines correspond to semiempirical fits using the Lassettre series.

CFC [5–7] and other CFHC molecules [8]. In addition to these major one-electron transitions, there are also small contributions from other configurations in these excited states that may introduce other orbital signatures to the GOS profiles. The good agreement between the calculated transition energies and the experiment has already provided some support for the above assignment. The term values of the $10a_1$ orbital derived from the present assignment (4.3–5.7 eV) are also in good accord with the term values of 3.9–6.2 eV obtained from a C $1s$ and Cl $2p$ inner-shell EELS study [41]. Furthermore, the sum of the calculated DOS values for the transitions to the $^1A_2$ (0.0000), ^1E (2×0.0152), $^1A_1$ (0.0013), and ^1E (2×0.0070) excited states gives a total oscillator strength of 0.0457, which is in fair agreement with the f_0 value of $\sim$0.0575 derived by fitting the GOS data to a Lassettre series (Table V). The discrepancy in the DOS between the single-excitation CI excited-state calculation and the experiment reflects the need for better quality wave functions especially for the excited states.

Like the n(Cl $3p$)$\rightarrow\sigma^*$(C-Cl) transitions in $CFCl_3$ [6] [Fig. 8(b)] and CCl_4 [5] [Fig. 8(c)], the GOS profile of the feature at 7.2 eV in $CHCl_3$ [Fig. 8(a)] contains both a strong maximum at $K\sim0$, characteristic of dipole-allowed transitions, and a secondary maximum at $K^2\sim0.9$ a.u., which is indicative of nondipole transitions. Based on symmetry consideration for C_{3v} molecules [49], the maximum at $K\sim0$ may be attributed to the dipole-allowed $9e\rightarrow10a_1$, $9a_1\rightarrow10a_1$ and $8e\rightarrow10a_1$ transitions. On the other hand, the maximum at $K^2\sim0.9$ a.u. may be due to the $2a_2\rightarrow10a_1$ transition, which is dipole forbidden but magnetic-dipole allowed. Figure 9 shows the wave-function densities of the relevant initial-state and final-state orbitals involved in the above transitions in a H-C-Cl (σ_v symmetry) plane (or, where appropriate, its perpendicular plane). The contour maps were generated from *ab initio* SCF wave functions obtained by GAUSSIAN 90 [35] with a 6-31G basis set and an internally optimized geometry. Evidently, the $10a_1$ orbital (LUMO) consists mainly of σ^* antibonding overlaps between the C $2s$ and Cl $3p$ orbitals [Fig. 9(b)]. The $2a_2$ orbital (HOMO) is mainly composed of Cl $3p$ nonbonding orbitals oriented perpendicularly to the C-Cl bond out of the σ_v plane [Fig. 9(c)]. The transition overlap for the $2a_2\rightarrow10a_1$ transition therefore occurs at the Cl sites and resembles that of an atomic $p\rightarrow p$ quadrupole transition in a Cl atom. In addition to the dominant Cl $3p$ orbitals perpendicular to the C-Cl bond in the σ_v plane, the $9e$ [Fig. 9(d)], $9a_1$ [Fig. 9(e)], and $8e$ orbitals [Fig. 9(f)] also consist of minor C $2p$ components. The overlaps between the minor C $2p$ components in these (initial-state) orbitals and the C $2s$ component in the $10a_1$ (final-state) orbital therefore contribute to the observed dipole components in the GOS profiles of the corresponding transitions, while the $p\rightarrow p$ overlaps at the

TABLE V. Comparison of the experimental and calculated values for the transition energy and dipole oscillator strength (f_0) of the 7.2-eV feature in $CHCl_3$.

		Excited state obtained by a single-excitation CI excited-state calculation with a 6-31G basis set[c]			
	Experiment	$^1A_2$ ($2a_2\rightarrow10a_1$)	^1E ($9e\rightarrow10a_1$)	$^1A_1$ ($9a_1\rightarrow10a_1$)	^1E ($8e\rightarrow10a_1$)
Transition energy (eV)	7.2±0.2[a]	7.219	7.516	7.592	7.953
f_0	0.0575±7%[b]	0.0000	0.0152 (2×)[d]	0.0013	0.0070 (2×)[d]
			Sum=0.0457		

[a]Peak maximum of the experimentally observed feature.

[b]This value is obtained semiempirically by fitting the GOS profile with a Lassettre series. The quoted error is derived from the fitting procedure only.

[c]The dominant configuration of the excited state is given in parentheses.

[d]The f_0 value corresponds to a single degenerate state and should be multiplied by the degeneracy shown in parentheses.

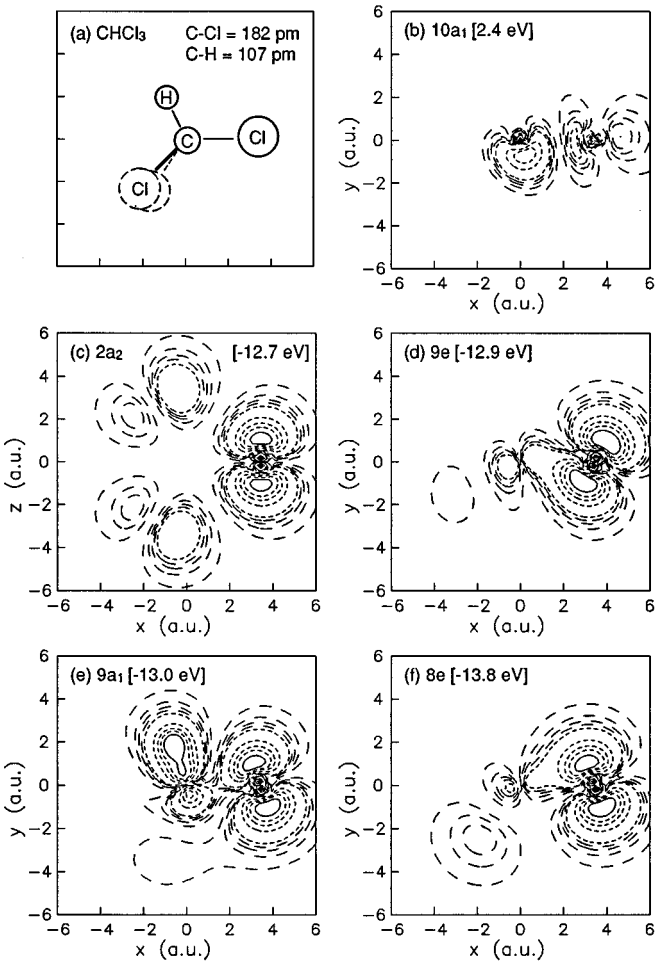

FIG. 9. Two-dimensional density contour maps for (b) the $10a_1$, (c) $2a_2$, (d) $9e$, (e) $9a_1$, and (f) $8e$ orbitals of $CHCl_3$. The contour maps are calculated using *ab initio* SCF wave functions of 6-31G quality [35] with an internally optimized geometry shown schematically in (a). The xz plane corresponds to a σ_v symmetry plane that contains one of the H-C-Cl groups with the carbon atom located at the origin. The contour values are 0.1%, 0.3%, 0.5%, 0.7% (dashed lines), 1%, 3%, 5%, 7% (dotted lines), 10%, 30%, 50%, 70%, and 90% (solid lines) of the maximum density. The calculated orbital energies are given in parentheses.

Cl sites again give rise to the nondipole components. This simple orbital picture is in qualitative accord with the DOS values given by the single-excitation CI excited-state calculation, which shows that the ''purely'' nondipole $2a_2 \rightarrow 10a_1$ transition has zero DOS and the other three dipole-allowed transitions have nonzero DOS values (Table V). Although the simple one-electron description is sufficient to qualitatively explain the nature of the transitions involved, *ab initio* GOS calculations involving accurate ground-state and excited-state wave functions are necessary in order to obtain a more quantitative understanding of the GOS profiles themselves.

Except for the differences in the contributions from the H and F atoms, the LUMO and the four HOMOs in $CHCl_3$ (Fig. 9) closely resemble the corresponding orbitals in $CFCl_3$ (Fig. 9 of Ref. [6]). Furthermore, the highly atomiclike nature of the electronic transitions involving these low-lying orbitals in $CHCl_3$ is found to be very similar to that of the previously reported $n(\mathrm{Cl}\ 3p) \rightarrow \sigma^*(\mathrm{C\text{-}Cl})$ transitions in $CFCl_3$ [6]. This similarity is also manifested in their corresponding GOS profiles (Fig. 8), particularly in terms of the ratio of the secondary maximum at $K^2 \sim 0.9$ a.u. (the nondipole component) to the maximum at $K \sim 0$ (the dipole component). However, the ''nondipole-to-dipole'' ratios for these transitions in $CHCl_3$ and $CFCl_3$ are found to be notably different from that of the corresponding low-lying feature in CCl_4 [5] [Fig. 8(c)], which suggests that molecular symmetry plays a key role in defining the contributions from different types of transitions to the GOS profile. In particular, the excited states of a more cagelike molecule such as CCl_4 may be more susceptible to distortion due to Jahn-Teller effects, which in turn give rise to the more intense $K \sim 0$ (dipole) peak in the corresponding GOS profile.

Our recent angle-resolved EELS studies show that the $n \rightarrow \sigma^*$ transitions in CFC and CFHC molecules studied to date contain significant nondipole contributions. Furthermore, simple potential-energy curve calculations suggest that most of these $n(\mathrm{Cl}\ 3p) \rightarrow \sigma^*(\mathrm{C\text{-}Cl})$ transitions, including in particular the $7e \rightarrow 11a_1$ transition at 7.7 eV in CF_3Cl [7], $(7a'',14a') \rightarrow 15a'$ transitions at 8.0 eV in CHF_2Cl [8], $(3a_2,8b_2) \rightarrow 13a_1$ transition at 6.9 eV in CF_2Cl_2, $10e \rightarrow 12a_1$ transition at 6.8 eV in $CFCl_3$ [6], and $2t_1 \rightarrow 7a_1$ transition at 7.2 eV in CCl_4 [5], could lead to dissociation of the C-Cl bond. The possible predissociative nature of the 7.2-eV feature in $CHCl_3$ is also investigated by examining the potential-energy curves, obtained by performing a similar single-excitation CI excited-state calculation as discussed above, along one of the C-Cl bond directions for the lowest-lying $^1A_2$, ^1E, $^1A_1$, and ^1E excited states. In particular, except for the single C-Cl bond length of interest, all other structural parameters obtained from the internally optimized geometries were held constant in the potential-energy curve calculation. The calculated potential-energy curves shown in Fig. 10 clearly indicate that a vertical transition originated from the ground vibrational state of the $X\ ^1A_1$ state terminates at the repulsive part of the potential-energy curve of the lowest-lying ^1E state (the $9e \rightarrow 10a_1$ transition). Although this simple potential-energy curve calculation only gives a qualitative one-dimensional view of the multidimensional potential-energy surfaces, it suggests that some of the $n(\mathrm{Cl}\ 3p) \rightarrow \sigma^*(\mathrm{C\text{-}Cl})$ transitions in $CHCl_3$, like the aforementioned $n \rightarrow \sigma^*$ transitions in CF_nCl_{4-n} $(n=0\text{–}3)$, may also lead to the breakage of the C-Cl bond.

IV. CONCLUDING REMARKS

In summary, we provide a detailed electron energy-loss study of the valence-shell electronic structure of CHF_3 and $CHCl_3$. The EELS spectra measured at 1° are in good agreement with the limited VUV photoabsorption data available in the literature. Using the term values obtained in an earlier inner-shell small-angle EELS study [41], we provide tentative assignments for some of the observed spectral features in $CHCl_3$. The present work also gives comprehensive angle-resolved EELS measurements, which show that the Bethe surfaces of these C_{3v} molecules are remarkably similar to those of their corresponding T_d homologs, CF_4 and CCl_4 [5]. Moreover, we determine the absolute GOS profiles for some of the more prominent low-lying preionization-edge electronic excitation and Rydberg features in CHF_3 and $CHCl_3$.

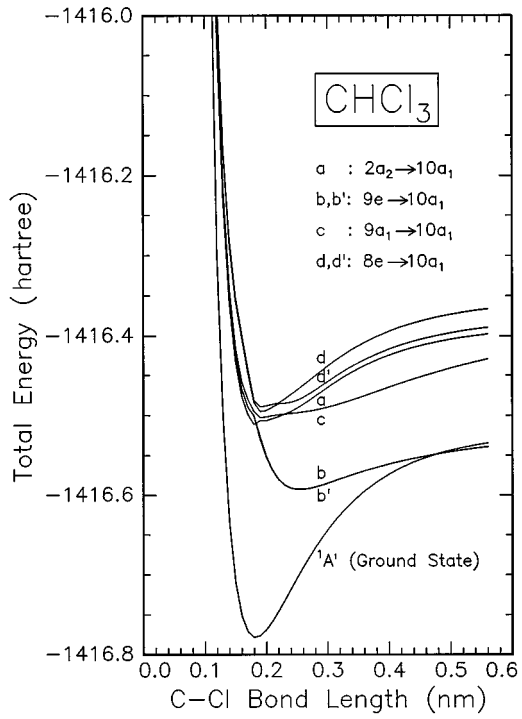

FIG. 10. Potential-energy diagram along the C-Cl bond direction for the ground-state $^1A_1$ and the four lowest-lying excited states, as indicated by their corresponding dominant one-electron transitions labeled as a, b (b'), c, and d (d'). The potential-energy curves are obtained by a single-excitation configuration-interaction excited-state calculation with a 6-31G basis set [35]. Except for one single C-Cl bond length, all other structural parameters obtained from an internal geometry optimization are held constant in the potential-energy curve calculation.

In particular, the GOS profiles of the lowest-lying preionization-edge Rydberg features in CHF_3 and $CHCl_3$ are evidently dominated by dipole interactions. Weak GOS secondary maxima (and minima) are found at a similar K position for these Rydberg features within the same molecule. Furthermore, these GOS secondary maxima (and minima) in $CHCl_3$ are observed at a lower K value than the respective extrema (of the corresponding Rydberg transitions) in CHF_3. The trend in these secondary extrema can be qualitatively understood by considering the spatial distributions of the overlap function between the predominantly nonbonding F $2p$ or Cl $3p$ initial-state orbitals and the diffuse final-state Rydberg orbitals. In addition, the GOS profile of the low-lying excitation feature at 7.2 eV in $CHCl_3$ is found to have a shape similar to the $n\rightarrow\sigma^*$ features in CCl_4 (and $CFCl_3$), which is also characteristic of a mixture of dipole-allowed and nondipole transitions. Based on the result of a single-excitation CI excited-state calculation, this low-lying feature can be attributed predominantly to the dipole-allowed $9e\rightarrow 10a_1$, $9a_1\rightarrow 10a_1$, and $8e\rightarrow 10a_1$ transitions (contributing to the GOS maximum at $K\sim 0$), and to a dipole-forbidden but magnetic-dipole-allowed $2a_2\rightarrow 10a_1$ transition (corresponding to the secondary maximum at $K^2\sim 0.9$ a.u.). In particular, the nondipole interactions of these transitions generally resemble that of an atomic $p\rightarrow p$ transition in a chlorine atom. Based on an orbital density analysis of the nonbonding HOMOs ($2a_2$, $9e$, $9a_1$, and $8e$) and the σ^* LUMO ($10a_1$), generated by using *ab initio* SCF wave functions, the n(Cl $3p$)$\rightarrow\sigma^*$(C-Cl) nature of this low-lying feature is demonstrated. In the case of the $9e\rightarrow 10a_1$ transition, a simple potential-energy curve calculation further suggests the "predissociative" nature of the lowest-lying ^1E excited state. Despite the usefulness of this kind of qualitative analysis, more detailed understanding of the nature of the excited states clearly requires more sophisticated (GOS) calculations.

ACKNOWLEDGMENTS

This work was supported by the Natural Sciences and Engineering Research Council of Canada.

[1] M. J. Molin and F. S. Rowland, Rev. Geophys. Space Phys. **13**, 1 (1975).
[2] *Plasma Reactions and Their Applications*, Japan Materials Report (Japan Technical Information Service, ASM International, Metals Park, OH, 1988).
[3] M. W. Yen, P. M. Johnson, and M. G. White, J. Chem. Phys. **99**, 126 (1993), and references therein.
[4] T. Ibuki, A. Hiraya, and K. Shobatake, J. Chem. Phys. **90**, 6290 (1989), and references therein.
[5] J. F. Ying and K. T. Leung, J. Chem. Phys. **100**, 7120 (1994).
[6] J. F. Ying and K. T. Leung, J. Chem. Phys. **101**, 8333 (1994).
[7] J. F. Ying, C. P. Mathers, K. T. Leung, H. P. Pritchard, C. Winstead, and V. McKoy, Chem. Phys. Lett. **212**, 289 (1993).
[8] J. F. Ying and K. T. Leung, J. Chem. Phys. **100**, 1011 (1994).
[9] J. Doucet, P. Sauvageau, and C. Sandorfy, J. Chem. Phys. **58**, 3708 (1973).
[10] G. C. King and J. W. McConkey, J. Phys. B **11**, 1861 (1978).
[11] R. S. Barbieri and R. A. Bonham, Phys. Rev. A **45**, 7929 (1992), and references therein.
[12] J. S. Lee, J. Chem. Phys. **67**, 3998 (1977).
[13] A. C. A. Souza and G. G. B. de Souza, Phys. Rev. A **38**, 4488 (1988).
[14] K. N. Klump and E. N. Lassettre, Chem. Phys. Lett. **51**, 99 (1977).
[15] K. N. Klump and E. N. Lassettre, J. Chem. Phys. **68**, 3511 (1978).
[16] R. Camilloni, E. Fainelli, G. Petrocelli, and G. Stefani, J. Phys. B **20**, 1839 (1987).
[17] H. M. Boechat Roberty, C. E. Bielschowsky, and G. G. B. de Souza, Phys. Rev. A **44**, 1694 (1991).
[18] J. F. Ying, C. P. Mathers, and K. T. Leung, Phys. Rev. A **47**, R5 (1993).
[19] M. Inokuti, Rev. Mod. Phys. **43**, 297 (1971).
[20] K. J. Miller, J. Chem. Phys. **59**, 5639 (1973).
[21] A. Skerbele and E. N. Lassettre, J. Chem. Phys. **52**, 2708 (1970); F. Hanne and J. Kessler, Phys. Rev. A **5**, 2457 (1972); T. C. Wong, J. S. Lee, and R. A. Bonham, Phys. Rev. A **11**, 1963 (1975); C. E. Bielschowsky, G. G. B. de Souza, C. A.

Lucas, and H. M. Boechat Roberty, *ibid*. **38**, 3405 (1988).
[22] K. J. Miller, S. R. Mielczarek, and M. Krauss, J. Chem. Phys. **51**, 26 (1969).
[23] S. R. Mielczarek and K. J. Miller, Chem Phys. Lett. **10**, 369 (1971).
[24] M. Krauss and S. R. Mielczarek, J. Chem. Phys. **51**, 5241 (1969).
[25] H. M. Boechat Roberty and G. G. B. de Souza, J. Phys. B **25**, 4641 (1992).
[26] F. H. Read and G. L. Whiterod, Proc. Phys. Soc. London **85**, 71 (1965).
[27] R. A. Bonham, J. Chem. Phys. **36**, 3260 (1962).
[28] Y. Kim, M. Inokuti, G. E. Chamberlain, and S. R. Mielczarek, Phys. Rev. Lett. **21**, 1146 (1968).
[29] R. A. Bonham, *Electron Spectroscopy: Theory, Techniques and Applications*, edited by C. R. Brundle and A. D. Baker (Academic, New York, 1979), Vol. 3, p. 127.
[30] J. F. Ying, T. A. Daniels, C. P. Mathers, H. Zhu, and K. T. Leung, J. Chem. Phys. **99**, 3390 (1993).
[31] Although the momentum transfer is not constant over the entire energy loss range in a typical EELS spectrum recorded at a fixed scattering angle, the variation of the momentum transfer with respect to the energy loss can be ignored if a sufficiently high impact energy is used. For the present experimental angular range (1°–9.5°), the corresponding momentum transfer is found to be effectively constant over our entire energy loss range (0–150 eV) at 2.5-keV impact energy.
[32] Y. Iida, F. Carnovale, S. Daviel, and C. E. Brion, Chem. Phys. **105**, 211 (1986).
[33] R. S. Barbieri and R. A. Bonham, Phys. Rev. A **44**, 7361 (1991).
[34] M. Inokuti, J. L. Dehmer, T. Baer, and J. D. Hanson, Phys. Rev. A **23**, 95 (1981), and references therein.
[35] M. J. Frisch, M. Head-Gordon, G. W. Trucks, J. B. Foresman, H. B. Schlegel, K. Raghavachari, M. A. Robb, J. S. Binkley, C. Gonzalez, D. J. Defrees, D. J. Fox, R. A. Whiteside, R. Seeger, C. F. Melius, J. Baker, R. L. Martin, L. R. Kahn, J. J. P. Stewart, S. Topiol, and J. A. Pople, GAUSSIAN 90, Revision F (Gaussian Inc., Pittsburgh, 1990).
[36] G. Bieri, L. Åsbrink, and W. von Niessen, J. Electron. Spectrosc. Relat. Phenom. **23**, 281 (1981), and references therein.
[37] W. von Niessen, L. Åsbrink, and G. Bieri, J. Electron. Spectrosc. Relat. Phenom. **26**, 173 (1982), and references therein.
[38] S. T. Manson, A. Msezane, A. F. Starace, and S. Shahabi, Phys. Rev. A **20**, 1005 (1979).
[39] W. R. Harshbarger, M. B. Robin, and E. R. Lassettre, J. Electron. Spectrosc. Relat. Phenom. **1**, 319 (1972).
[40] F. C. Brown, R. Z. Bachrach, and A. Bianconi, Chem. Phys. Lett. **54**, 425 (1978).
[41] A. P. Hitchcock and C. E. Brion, J. Electron. Spectrosc. Relat. Phenom. **14**, 417 (1978).
[42] S. Stokes and A. B. F. Duncan, J. Am. Chem. Soc. **80**, 6177 (1958).
[43] P. Sauvageau, R. Gilbert, P. P. Berlow, and C. Sandorfy, J. Chem. Phys. **59**, 762 (1973).
[44] L. C. Lee, J. C. Han, C. Ye, and M. Suto, J. Chem. Phys. **92**, 133 (1990).
[45] C. R. Zobel and A. B. F. Duncan, J. Am. Chem. Soc. **77**, 2611 (1955).
[46] M. B. Robin, *High Excited States of Polyatomic Molecules* (Academic, New York, 1985), Vol. 3; see also *ibid*. (Academic, New York, 1974), Vol. 1.
[47] E. N. Lassettre, J. Chem. Phys. **43**, 4479 (1965); M. A. Dillon and E. N. Lassettre, *ibid*. **62**, 2373 (1975).
[48] D. A. Shaw, G. C. King, F. H. Read, and D. Cvejanovic, J. Phys. B **15**, 1785 (1982).
[49] G. Herzberg, *Molecular Spectra and Molecular Structure* (Van Nostrand, Toronto, 1966), Vol. III.